Traction Force Measurements of Human Aortic Smooth Muscle Cells Reveal a Motor-Clutch Behavior

Claudie Petit, Alain Guignandon, Stéphane Avril

Tech Science Press

Traction Force Measurements of Human Aortic Smooth Muscle Cells Reveal a Motor-Clutch Behavior

Petit Claudie[1], Guignandon Alain[2] and Avril Stéphane[1,*]

[1]Mines Saint-Etienne, Université de Lyon, INSERM, U 1059 SAINBIOSE, F-42023 Saint-Etienne, France.
[2]Université Jean Monnet, Université de Lyon, INSERM, U 1059 SAINBIOSE, F-42023 Saint-Etienne, France.
[*]Corresponding Author: Avril Stéphane. Email: avril@emse.fr.

Abstract: The contractile behavior of smooth muscle cells (SMCs) in the aorta is an important determinant of growth, remodeling, and homeostasis. However, quantitative values of SMC basal tone have never been characterized precisely on individual SMCs. Therefore, to address this lack, we developed an *in vitro* technique based on Traction Force Microscopy (TFM). Aortic SMCs from a human lineage at low passages (4-7) were cultured 2 days in conditions promoting the development of their contractile apparatus and seeded on hydrogels of varying elastic modulus (1, 4, 12 and 25 kPa) with embedded fluorescent microspheres. After complete adhesion, SMCs were artificially detached from the gel by trypsin treatment. The microbeads movement was tracked and the deformation fields were processed with a mechanical model, assuming linear elasticity, isotropic material, plane strain, to extract the traction forces formerly applied by individual SMCs on the gel. Two major interesting and original observations about SMC traction forces were deduced from the obtained results: 1. they are variable but driven by cell dynamics and show an exponential distribution, with 40% to 80% of traction forces in the range 0-10 μN. 2. They depend on the substrate stiffness: the fraction of adhesion forces below 10 μN tend to decrease when the substrate stiffness increases, whereas the fraction of higher adhesion forces increases. As these two aspects of cell adhesion (variability and stiffness dependence) and the distribution of their traction forces can be predicted by the probabilistic motor-clutch model, we conclude that this model could be applied to SMCs. Further studies will consider stimulated contractility and primary culture of cells extracted from aneurysmal human aortic tissue.

Keywords: Cell biomechanics; aortic aneurysm; mechanotransduction; mechanosensitivity; smooth muscle cells (SMC); fluorescent microscopy (FM); traction force microscopy (TFM); isolated cells

1 Introduction

It is now widely acknowledged that the biomechanical behavior of smooth muscle cells (SMCs) in the aorta, through mechanosensitivity and mechanotransduction, is an important determinant of growth, remodeling, and homeostasis [1-7].

Aortic SMCs are highly sensitive to:

-biochemical [8-13].

-and mechanical stimuli from the surrounding extracellular matrix (ECM) [2,14-19].

In pathologies such as aortic aneurysms, the function of aortic SMCs may be altered by:

-genetics ([20-28]),

-hemodynamics ([29,30]),

-or biomechanics ([3,21,31]),

This may induce manifestations such as

-SMC apoptosis [16,32,33].

-or phenotype switch from a mature quiescent and contractile phenotype towards a synthetic one [2,6,9,10,19,34].

A synthetic SMC is able to proliferate and migrate more than a contractile one. It can induce ECM synthesis and degradation [4,17,19,28]. This remodeling of the aortic structure is often irreversible, with

-a permanent change of mechanical properties [2,4,14,15].

-and possible vulnerability to rupture [29,35,36].

Moreover, synthetic SMCs lose their contractile abilities and are no longer able to contribute actively to the wall biomechanics [3,17,19,20,26].

Nevertheless, they can synthesize collagen fibers that compensate possible damage to elastic fibers, which are not renewed in adulthood [14,19,37-40].

This may lead to a vicious circle as elastin is required for the development of the contractile apparatus in SMCs [11,41].

At homeostasis, SMCs tend to have a basal tone through their contractile behavior which maintains a preferred tension on the ECM [3,26,40]. Any biochemical and biophysical imbalance may alter this tension, and this may lead to a vicious circle. In this way, the SMC is a fundamental key player of aortic biomechanics and mechanobiology [3,7,42]. However, quantitative values of SMC basal tone have never been characterized precisely.

In summary, there is a pressing need to investigate the biomechanical behavior of isolated cell, and particularly on human primary SMCs, as most of published studies:

-focused on animal SMCs [43-45].

-and characterized only biological markers of SMC contractility such as Alpha Smooth Muscle Actin (α-SMA), myosin light chain, or calcium entry and release [20,23,39,46,47].

The only study ever published to our best knowledge on mechanical quantification of contractility in human primary aortic SMCs is by Hall et al. [48].

This study was based on the traditional traction force microscopy (TFM) technique, which did not permit to focus on individual cells. In the present study, we present an augmented TFM technique to measure the traction forces applied by individual SMCs and relate them to relevant biological data about the contractile apparatus. After describing the new methodology in large details, from development to validation, we show original results quantifying the adaptation of aortic SMCs contractility to the substrate stiffness.

2 Material and Methods

2.1 Cell Culture

For this study, we used Aortic Smooth Muscle Cells from a human lineage (AoSMC, Lonza). After thawing, cells were put in culture in a T-75 flask for an entire week in a medium (SMGM-2, Lonza) promoting proliferation thanks to high (10%) fraction of Fetal Bovine Serum (FBS) and other specific components including growth factors. The cells were incubated at 37°C and 5% CO_2 to maintain the pH at 7.2-7.4.

In our study, SMCs were used between passages 4-7, and cultured one week more in a basal medium (SmBM, Lonza), containing low (2%) FBS and 0.04% heparin, according to the manufacturer's instructions.

Since they were from primary culture, AoSMCs were delivered at third passage, and therefore they reached passage 5 after two weeks of culture. Firstly, the cells were passaged at the end of the first week when they reached 70-80% confluence in growth medium, and transferred in three other T-75 flasks containing basal medium that reduced their proliferation. As primary cells are particularly sensitive, HEPES-Buffered Saline Solution (HEPES-BSS) (ReagentPack, Lonza) was used instead of standard

Phosphate Buffered Saline (PBS) for a softer initial cell washing and low trypsin (0.025%)-EDTA solution (ReagentPack, Lonza) was used to break down the focal adhesions in the culture dish. Once they reached 50-70% confluence in basal medium (approximately one week), the cells could be used both for another subculture or for sample preparation at fifth passage.

2.2 Sample Preparation and Staining

We observed firstly the cell internal architecture with fluorescent microscopy, and particularly the α-SMA expression that constitutes the contractile thin filaments. We used fluorescent staining on fixed AoSMCs adhering to a CYTOO™ fibronectin coated chip (Fig. 1(B)). All the fluorescent dyes and staining protocol are detailed in Appendix A.

For the TFM tests, previously starved AoSMC (see Subsection 2.1) were transferred in the 24-well plates containing ready-to-use hydrogels with different stiffness properties (Cell Guidance System, Softwell™ 24, collagen pre-coated, Softrack 0.2 µm diameter microbeads labelled with yellow-green fluorescent dye) (Fig. 1(A)). Then, we used 24-well plates of intermediary stiffness values: 4, 8, 12 and 25 kPa for our experiments. These hydrogels were made of a 400µm-thick layer of polyacrylamide, which was assumed to be linear elastic under the range of strains considered in our study. The gel dimensions (12 mm diameter) were assumed to be infinitely large with respect to the cell size. Moreover, athe collagen I coating added during the manufacturing process provides a ready-to-use physiological surface for cell adhesion and culture.

Cells were incubated in basal medium two days before TFM experiments, providing an amount of 10 000 per well which seemed not to saturate the gels. Two days were sufficient for a good spreading of SMCs, which adopted their specific elongated spindle shape. This shape was a good indicator of fully contractile SMCs, unlike synthetic ones, as they tend to exert traction forces along their length. That is the reason why we introduced the morphological criterion of "spindle-shapeness" that corresponds to the ratio between the wider part of the cell (around the nucleus) and its length. Cells at low passages (4-7) and cultured in basal medium tend to elongate more, making these specific conditions well suited for our TFM experiments.

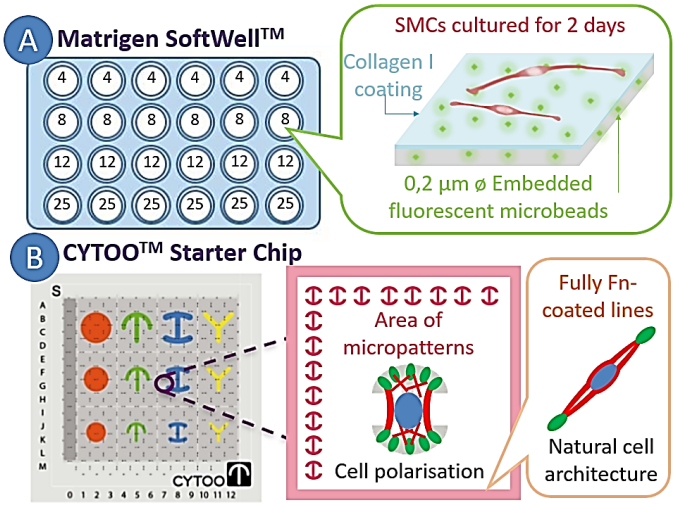

Figure 1: A) The Matrigen 24-well plate consists in 4 lines of 6 hydrogel samples with the same stiffness. The gels are delivered with a collagen I adhesive pre-coating and yellow-green fluorescent microbeads whose diameter is 0.2 µm, B) The CYTOO chip is divided into several areas of fibronectin (Fn) adhesive micropatterns, where the cell architecture is constrained to polarize according to the shape of the pattern. Each area is surrounded by fully Fn-coated lines where the cells adhere with a natural shape

2.3 Traction Force Microscopy (TFM) to Measure SMC Basal Tone

Previously cultured gels were put under a Carl Zeiss Axio Observer.Z1 station with the Zen software while remaining incubated at 37°C, 5% CO_2 in a chamber. The gels were firstly imaged through the GFP (Green Fluorescent Protein) channel to adjust the focus on the fluorescent microbeads that are already labelled with a Yellow-Green fluorophore. Then we used the phase contrast channel to look at the cell morphology and orientations. The best magnification was obtained with the Plan-Neofluar 20x/0.4 objective, which resulted in a resolution of 0.323 μm per pixel. This resolution was kept for all further data processing (see Subsection 2.4.1).

The method consisted in provoking SMC detachment from substratum using trypsin. The medium was first removed from the well and the cells were gently washed once with warm PBS, as some medium components tended to inhibit the trypsin effect. A little amount of PBS remained in the dish in order to keep the cells hydrated. The field of view of the objective allows for selecting an area of interest around 2-4 cells per well showing a clear spindle shape. Then the beads were imaged through the GFP channel that served also as a reference for the autofocus throughout the whole experiment. The autofocus enabled keeping the correct focus although other liquids were added to the medium. That was useful in our case when we added gently the trypsin solution at the third stage of the experiment. We paid attention not to touch the border of the well plate with the syringe, because any horizontal displacement could compromise the whole experiment. Then, the cells were let in trypsin until the end of the experiment. Normally, cells detached from the gels after a minute or two, and a deformation was observed in the gel with localized motions of the microbeads. The positions of microbeads were tracked during 5 min with a frequency of 1 frame per 30 s. Once the cells were detached by trypsin treatment, the well is not reusable. This process was therefore repeated on every well of the plate successively.

2.4 Traction Force Fields

2.4.1 Extracting the Experimental Displacement Fields

After acquisition, images were processed using the Zen software for contrast adjustment of the GFP channel on the microbeads, and were exported in TIFF format. We chose to export individually images of both the phase contrast and GFP channels, the first one for locating the cells and the second one for measuring gel deformations (See Subsection 3.2). The latter was achieved with the Digital Image Correlation (DIC) method, which is based on maximization of a cross-correlation criterion between images in reference and deformed states. The DIC algorithm is detailed in Appendix B.

2.4.2 Generating Theoretical Displacement Fields

Green functions are the expressions of displacement fields for a concentrated force. Given their slender shape, contractile SMCs apply traction forces along their length axis, making an angle θ with the x axis of the global coordinate system. Actions in the z direction (normal to the surface of the gels) are also neglected. Therefore, the force vector may be written:

$$F(x_0, y_0)\begin{Bmatrix}\cos(\theta)\\ \sin(\theta)\end{Bmatrix} \tag{1}$$

where $F(x_0, y_0)$ is the unknown traction force applied at (x_0, y_0). Videomicroscopy images of the phase contrast channel were used to estimate θ for each cell in our experiments. For any ROI, the displacement fields may be related to $F(x_0, y_0)$ with the Green functions such as:

$$\begin{Bmatrix}u(x,y)\\ v(x,y)\end{Bmatrix} = \begin{bmatrix}Gr_{xx}(x-x_0, y-y_0) & Gr_{xy}(x-x_0, y-y_0)\\ Gr_{xy}(x-x_0, y-y_0) & Gr_{yy}(x-x_0, y-y_0)\end{bmatrix}\begin{Bmatrix}\cos(\theta)\\ \sin(\theta)\end{Bmatrix} F(x_0, y_0) \tag{2}$$

where u and v are the displacement components at (x, y), F_x and F_y are the force components for a concentrated force at (x_0, y_0) and Gr_{ij} are the Green function components.

Assuming plane strains and assuming that the Boussinesq theory for an infinite isotropic half-space [49] was relevant here (thickness of Matrigen's gel is about 400 µm whereas adhesion forces are concentrated on surfaces of units of µm²), we obtained:

$$Gr_{xx} = \frac{1+\nu}{\pi E}\left(\frac{1-\nu}{r} + \frac{\nu}{r^3}x^2\right) \quad Gr_{xy} = \frac{1+\nu}{\pi E}\left(\frac{\nu}{r^3}xy\right) \quad Gr_{yy} = \frac{1+\nu}{\pi E}\left(\frac{1-\nu}{r} + \frac{\nu}{r^3}y^2\right) \tag{3}$$

where $= \sqrt{(x-x_0)^2 + (y-y_0)^2}$, ν is the Poisson ratio of the gel and E is the Young's modulus.

2.4.3 Deducing the Local Traction Force Value

From every ROI, to find the traction force applied by a single cell (Fig. 2(A)), we had to adjust the displacement fields predicted by the Green function against the experimental displacements obtained by DIC. As displacement fields may be subject to rigid body motions, we decided to work with strain fields (Fig. 2(B)).

We performed a tensor rotation to express the strains in a rotated coordinate system where the first axis (direction 1) was aligned with the cell axis (θ direction) (Fig. 2(C.1)). We derived the strain component $\overline{\varepsilon_{11}}$ (Fig. 2(C.2) resulting from a unit force by differentiation of Eq. (2) and adjusted it against the same strain ε_{11} component derived from DIC measurements (Fig. 2(C.1)). Then, the traction force was obtained as:

$$F(x_0, y_0) = \frac{\sum_{n=1}^{N_{\mathrm{ROI}}}[\varepsilon_{11}(x_n,y_n) * \overline{\varepsilon_{11}}(x_n,y_n)]}{\sum_{n=1}^{N_{\mathrm{ROI}}}[\overline{\varepsilon_{11}}(x_n,y_n) * \overline{\varepsilon_{11}}(x_n,y_n)]} \tag{4}$$

where (x_n, y_n) denote all the pixels of the ROI, $1 \le n \le N_{\mathrm{ROI}}$.

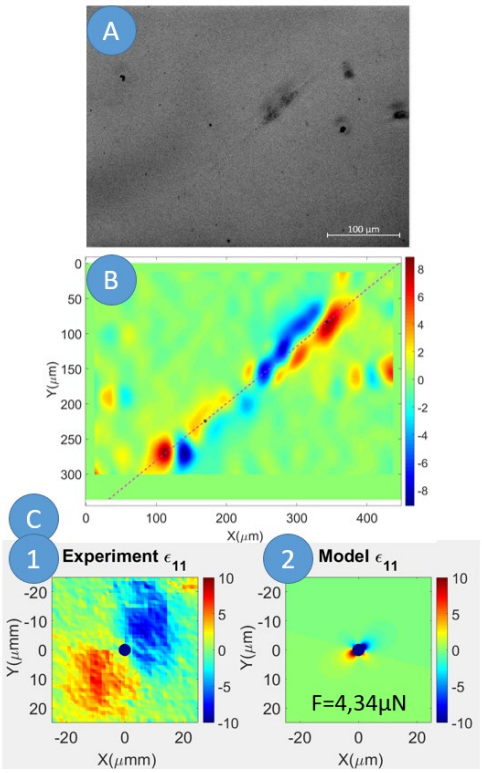

Figure 2: A) Image in phase contrast of a single cell binding to the gel. Microscope Axio Observer.Z1/7, Objective LD Plan-Neofluar 20x/0.4 Korr Ph 2 M27. Image size: 1040 × 1388 px, B) Strain field E11 measured after debonding of the same cell on a gel of stiffness 4 kPa. Experimental (C.1) and theoretical (C.2) strain fields obtained by tracking the motion of fluorescent microbeads with DIC after debonding of AoSMC. Because C.2 has to be multiplied by the calculated force to obtain C.1 (Eq. (4)), the figures show normalized strain fields

2.4.4 Model Validation and Verification

As our method was based on an analytical solution, we performed a validation using simulated data obtained with a 3D Finite Element (FE) model of the gels, on which we applied a concentrated force along the x direction.

The gel was modelled as a 5 × 5 × 0.4 mm^3 parallelepiped in the Abaqus® software. A quadratic tetrahedral mesh was defined with refinement along the z direction and around the central point in order to have a sufficient resolution near the concentrated force. The mesh consisted of 425747 elements and 583726 nodes for the half parallelepiped (symmetric boundary conditions were assumed with respect to the x-axis).

The material was assumed to have a linear elastic behavior and to remain nearly incompressibility (ν = 0.45). Forces were applied in the (x,y) plane (upper surface of the gel), at the central node of the mesh. Then we interpolated the displacement values on a grid mimicking the pixel grid of experimental measurements. After deriving the strain fields, we applied Eq. (4).

We validated the use of the analytical solution with the FE model. We obtained deformation fields resulting from a local force of 0.2 µN with different orientations. In Tab. 1, we report the forces obtained from Eq. (4) with the data generated by these FE models. An excellent agreement with the true value of the force was obtained, showing that the plane strain assumption of the model used in Eq. (4) was valid.

Table 1: Traction forces obtained with FE simulated strain data for different orientations of the applied force

Theta (°)	0	20	30	45	60	75	85	**Mean**
Force (N)	2.0306 × 10^{-7}	2.0243 × 10^{-7}	2.0268 × 10^{-7}	2.0064 × 10^{-7}	1.9958 × 10^{-7}	1.9969 × 10^{-7}	1.9856 × 10^{-7}	2.0095 × 10^{-7}

2.5 Statistical Analysis

We performed statistical analysis on the TFM measurements from the 24-well plates. This sample format allowed to obtain the cell traction force values on 6 wells of each stiffness value (4, 8, 12 and 25 kPa), and to increase the number of measurements. We used a Mann-Whitney non-parametric test in order to compare the distribution of two independent samples, with different sample size. The null hypothesis is that data from the two tested populations are from continuous distributions with equal medians. We tested our four populations two by two successively and displayed the results as a boxplot using Matlab®. The significance was stated when the p-value remain inferior to 5%, namely when the null hypothesis is rejected at this significance level.

For this second series of experiments, we also examined the distribution of the traction force values according to each gel stiffness by plotting histograms in Matlab®. These histograms represented the probability according to ten classes of forces between 0 and 100 µN. Then, we fitted them with an exponential law such as:

$$y_{model} = \lambda e^{-\lambda x} \tag{5}$$

where x represents a random variable and y is its distribution, while λ is a parameter to be determined, which corresponds to a simplification of the motor-clutch model (Eq. (8), Eq. (9)).

The experimental data were fitted using the Levenberg-Marquardt algorithm in Matlab®. More specifically, the fitting algorithm was applied between the experimental data x_{exp} and y_{exp}, respectively central position of each bar of the histogram and its related probability. Then, after identifying the optimal λ parameter, the results yielded the theoretical x_{mod} for every traction force value x_{exp}.

3 Results

3.1 SMC Morphology

The morphology of AoSMCs showed a pronounced uniaxial spindle-shape with low mean cellular

area on the hydrogels coated with collagen (Fig. 3(A)). Conversely, a non-elongated shape and large mean cellular area would indicate a hypertrophic morphology, characteristic of the synthetic phenotype [50]. The spindle-shapeness was measured on 120 cells used in the TFM experiments. The mean value, standard deviation, minimal and maximal values are reported in Tab. 2 below:

Table 2: Mean value, standard deviation, minimum and maximum

Mean	StD	Min	Max	N
0.0719	0.0332	0.0126	0.2824	120

On the CYTOO^{TM} chips, SMCs still presented in most cases an elongated shape and were randomly spread on the fully fibronectin coated line of the chip (Fig. 3(B)). But SMCs also tended to spread naturally in other directions depending on the pattern of fibronectin coating (Fig. 3(B)). On CYTOO^{TM} micropatterns, the cell could not develop focal adhesions out of the fibronectin coating due to the cytophobic PEG coating out of the fibronectin. Fluorescent imaging of these cells allowed to superimpose the two actin isoforms namely F-Actin and α-SMA and showed that the α-SMA specific isoform of SMCs was concentrated into long thin fibers all along the cell length (Fig. 3(B)). The F-Actin was dispersed into the whole cell volume and defined the cell shape (Fig. 3(B)). The CYTOO^{TM} chips remain useful even if they have not the same stiffness than the hydrogels, because we do not use them for quantitative mechanical measurement, but for cell component localization, cell polarization, and for assessment of the α-SMA expression in SMCs adhering on a 2D environment. The main advantage of the the CYTOO chip is to provide different mechanical environments, and we can observe the polarization of its cytoskeleton according to each of them. The aim is to show that the SMC's cytoskeleton is particularly dense around the focal adhesion at the ending parts of the cell, and forms long stress fibers concentration at each side of the cell. On the hydrogels, the cells freely adhere to the collagen coating, and we can relate this observation with CYTOO results in order to localize the cell components.

In the following, TFM experiments have been achieved only on AoSMCs adhering to hydrogels coated with collagen. These SMCs were artificially detached from the collagen by a trypsin treatment, which removed the traction forces they exerted on the gel initially. These forces were localized on the focal adhesions and oriented according to the direction of the α-SMA thin filaments (See Subsection 3.2).

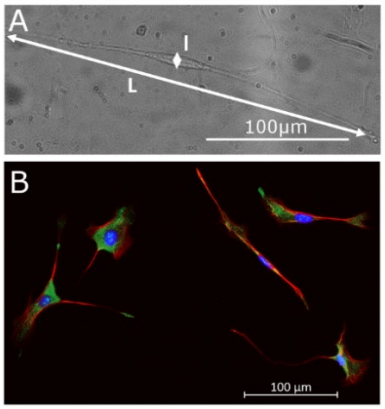

Figure 3: Observation of cell morphology and internal architecture for human aortic SMCs (AoSMC, Lonza). The cells were observed in phase contrast on a soft hydrogel (A) The cells were observed with fluorescent microscopy on a CYTOO^{TM} fully coated line (B). The spindle-shapeness corresponds to the ratio between the wider part of the cell (l) and its length (L) on uniaxial SMCs

3.2 First TFM Experiments with Trypsin Forced-Detachment

We showed in Fig. 2(B) typical strain patterns obtained after AoSMC forced-detachment due to trypsin. It can be noticed that the patterns showed two hotspots of strain around each focal adhesion, each hot spot

being nearly semicircular. One hotspot is blue and relates to the gel under compression, whereas symmetrically, the other hotspot is red and relates to the gel under tension. If we plot a line joining the center of both associated hotspots, we notice it is aligned with the AoSMC, confirming that traction forces are well aligned with the AoSMC main axis.

Applying Eq. (4) onto these strain fields, we could measure the traction forces on gels of different elastic moduli (from 0.5 to 50 kPa).

We noticed during previous experiments that gels with very low stiffness, such as 0.5, 1 or 2 kPa, presented several cracks after cell seeding, as shown in Fig. 4(A). That was not the case for the gels over 4 kPa (Fig. 4(B)). These cracks disturbed the uniform distribution of the fluorescent microbeads and could induce artifacts in force assessment. Conversely, the stiffest gel (50 kPa) presented lower deformations due to their stiffness, resulting in lower signal to noise ratios for the DIC method. AoSMC seem to have higher traction forces compared to fibroblasts (10-30 nN) or cardiomyocytes (70 nN) previously tested on 12 kPa substrates by Balaban et al. [51]. But AoSMCs also revealed higher traction forces than stem cells (0-200 nN [52]) or neurons (0.01-10 nN [53]) for instance. In fact, the cells adapt to the stiffness of their substrate, and stem cells tend to differentiate into neurons-like cells on substrates that have an elastic modulus close to those of the brain (0.1-1 kPa) or myoblast-like on intermediate stiffness (around 17 kPa) [52]. This may explain why gels with low stiffness properties, far from the natural stiffness of arteries, were inappropriate here for AoSMCs.

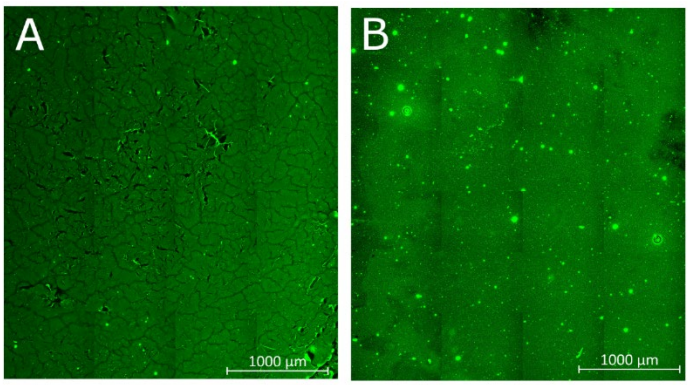

Figure 4: The most compliant gels (0.5, 1, 2 kPa, (A): 0.5 kPa) presented several cracks after cell seeding, but not the stiffest gels (from 4 to 50 kPa, (B): 25 kPa). Microscope Axio Observer.Z1/7, Objective Ec Plan-Neofluar 10x/0.30 Ph1. These images consist in 25 tiles each, which are merged by postprocessing in the Zen 2.3 Software. The black lines are due to a difference of exposure on the different tiles

Finally, this first analysis showed that optimal measurements of adhesion forces could be obtained for gel stiffness varying in a range between 4 kPa and 25 kPa. That is the reason why we chose this range of stiffness values for the design of the well plates.

A statistical analysis was performed for these experiments on the intermediate stiffness values (4, 8, 12 and 25 kPa) of the well plates. For each of the wells, we measured the adhesion forces for about 1 to 4 cells. For each cell, N measurements were achieved, where the displacement field showed the specific traction/compression pattern, namely at the anchorage points of the cell that have been affected efficiently by the trypsin. We plotted the traction force values individually according to each stiffness value, and the distributions are compared thanks to the Mann-Whitney non-parametric test. These results are given in Fig. 5 below:

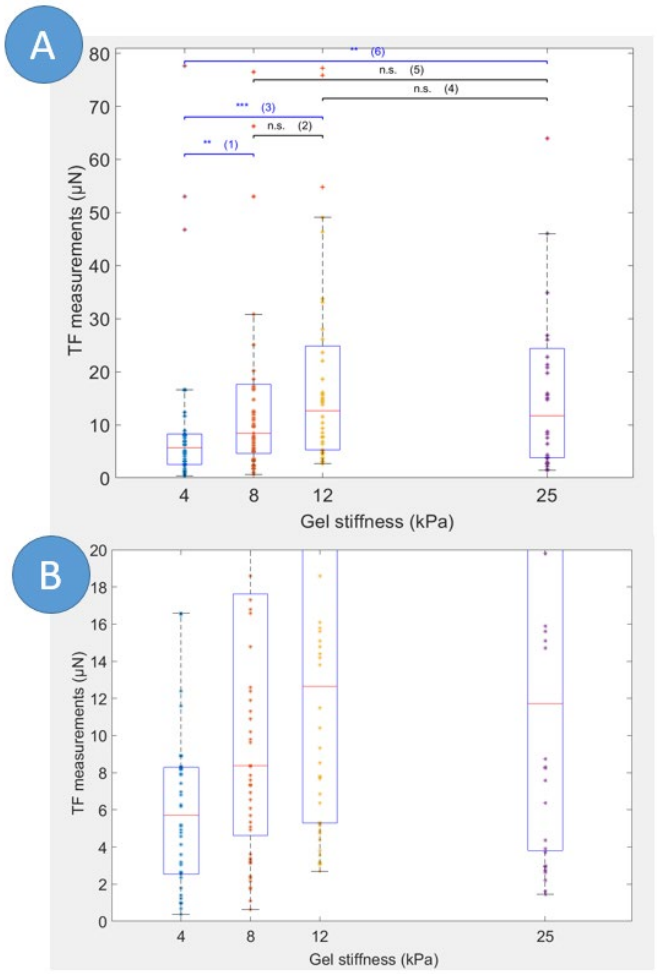

Figure 5: Cell traction force (TF) values obtained for different gel stiffness on 24-well plates for 0-80 µN range (A) and 0-20 µN (B). Even if only one gel was used for each stiffness value (4, 8, 12, and 25 kPa), 46, 49, 44, and 32 measurements were performed respectively on different focal adhesion sites and a number of cells between 1 and 4 per well. Significance was found using a Mann-Whitney test for (1), (3) and (6). Corresponding *p*-values: (1) 0.0090, (2) 0.2796, (3) 0.0003, (4) 0.6472, (5) 0.5985, (6) 0.0073. Significance level: * $p > 0.05$, ** $p < 10^{-2}$, *** $p > 10^{-3}$, n.s.: non-significant

3.3 Measurement of Cell Traction Force

Three 24-well plates containing 6 wells of each stiffness values (4, 8, 12, 25 kPa) were used to measure AoSMC adhesion. For each of these wells, we measured the adhesion forces for about 1 to 4 cells depending on their location. For each stiffness value, we could finally evaluate the traction forces for a number of cells varying between 30 and 50.

For some of them, we chose several measurement points on the same cell, considering different points where the unbinding focal adhesion led to a clear traction-compression pattern. Results are reported in Appendix C (Tab. C1). There is a rough increase of mean adhesion forces with the stiffness, although the mean force value for 8kPa is very close to the one of 25 kPa. Moreover, standard deviations are relatively large and the difference of adhesion forces between each stiffness are not significant.

Histograms of the adhesion forces highlight the variable behavior of adhesion forces (Fig. 5). The distribution is an exponential distribution. Depending on the stiffness, between 40 to 80% of cells have adhesion forces below 10 µN, but a fraction of them have adhesion forces that can go up to 50 or 60 µN.

As the adhesion forces do not follow a normal distribution, it is not possible to analyze the means in Tab. C1 to compare the different stiffness properties.

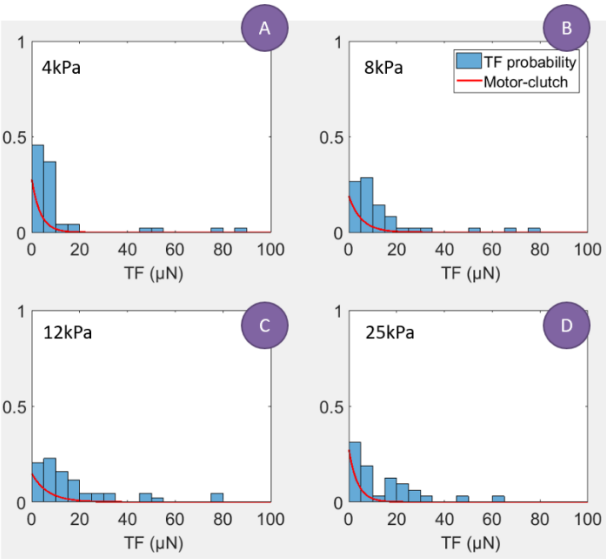

Figure 6: Histograms showing the probability distribution of the measured traction forces (TF) for each stiffness value: A) 4 kPa, B) 8 kPa, C) 12 kPa, D) 25 kPa (width of each bar: 10^{-5}N). The red curves represent the fitted exponential motor-clutch model

By fitting the distribution of adhesion forces with an exponential function (Fig. 6), we identified the λ parameter of Eq. (5) for each stiffness. Values are reported in Tab. 3 below:

Table 3: Fitting coefficient according to the substrate stiffness

Stiffness (kPa)	λ
4	0.2766
8	0.1896
12	0.1487
25	0.2749

It can be noticed that the λ parameter increased for stiffness varying between 4 kPa and 12 kPa. This is in agreement with histograms showing that the distribution shifted progressively from lower to higher adhesion forces when the stiffness was increased. In other words, when the stiffness increased, the fraction of cells having adhesion forces higher than 10 μN was increased. However, for the 25 kPa stiffness, there was no significant difference compared to 12 kPa.

These results showed that the substrate stiffness impacted significantly the adhesion forces of AoSMCs. Higher adhesion forces were obtained for the 12 kPa substrate.

4 Discussion

4.1 Preserving the Contractility of SMC

In the current study, we studied the contractile behavior of AoSMCs from human primary culture delivered at third passage and used at passages 5 to 7. This range of passages did not affect significantly the cell contractility as shown in a previous study from Murray et al. [54]. All conditions ensured sufficiently fresh and healthy cells (i.e., not from too many subdivisions) to generate a significant contractility.

SMCs may be subject to phenotypic switch [10,38,55], from contractile to synthetic which is the phenotype of early aortic development [8,9,13]. Consequently, we avoided phenotypic switching by adapting the cell culture conditions. More specifically, we followed the supplier's instructions for cell culture in order to preserve the maximal contractile abilities of the cells, using a differentiation medium containing low FBS and heparin. If both the heparin [17,56] and the serum starvation have an influence on the cell quiescence, only the starvation affects its contractility [57,58]. This is a crucial point for mechanical experiments on single SMC.

Good indicators for a well-preserved contractile behavior of AoSMCs were also their clear spindle-shape on hydrogels and the high expression of specific actin isoform α-SMA [50] under the shape of long thin filament all along the cell length. These filaments are well known for their high contractility and are present only in cell types that need to contract strongly in the human body, like myofibroblasts and SMCs [20,46,59].

We have found a significant effect of the substrate stiffness on the adhesion forces generated by cells and measured using TFM. Under stress free conditions, normal aortic walls have a stiffness around 40 kPa and increase until 110 kPa in atherosclerosis [43]. The stiffness can reach several MPa in pressurized arteries. Therefore, the Matrigen^{TM} substrates used in our study, having elastic modulus in the range 0.5 to 50 kPa, are more compliant than a normal aortic wall. However, it is difficult to extrapolate *in vivo* conditions to 2D *in vitro* culture and we found that AoSMCs showed the most interesting stiffness dependence between 4 and 25 kPa.

Not only the stiffness is important but also the composition of the substrate (binding proteins), with respect to cell adhesion. We have used pre-coated gels with type I collagen. The cells seemed to keep a very elongated shape on this type of coating. Previous studies have interpreted the SMC spindle shape as a preservation of its contractile phenotype [60,61]. Other studies highlighted the diversity of SMC responses depending on the type of binding proteins used in the substrate, such as fibronectin or laminin [10,62,63]. If the fibronectin is mainly present in the ECM of blood vessels during early development and seems to induce SMCs proliferation, migration and ECM synthesis [8,9], the laminin is required further for SMCs maturation towards a contractile phenotype [13]. Fibrillar type I collagen is naturally present in the media [60] and SMCs tend to align along collagen fibrils [64]. Collagen seems to reduce the cell proliferation on softer gel (25 kPa) relatively to stiffer one (135 kPa) or soft gel coated with laminin [43]. SMCs also tend to align naturally with the direction of maximum principal stress [2,64,65]. Moreover, another study has already investigated the regulation of the focal adhesions on type I collagen in response to a vasoactive agonist [37]. Hence, since we tried to define suitable biological conditions to preserve SMC contractility, type I collagen coating remains relevant for TFM experiments. Further investigations could consider gels with fibronectin or laminin instead of simply collagen I. We did some preliminary tests of ASMC culture on fibronectin, which showed multidirectional spreading of SMCs (Fig. 2(B)), tending to confirm that fibronectin may promote phenotypic switching towards synthetic SMCs [10,13,62,63].

Another important aspect of our experiments is the highly photosensitive behavior of AoSMCs [66,67]. Even when not exposed to bright light, they have demonstrated the same effect with fluorescent light on Hoescht channel [67,68]. And since the Hoescht stain of the nuclei requires an UV excitation wavelength, TFM experiments will always induce some damage to exposed SMCs. A special attention was paid to avoid exposing twice the same area in successive experiments.

4.2 Traction Force Measurements

The measured adhesion forces are in good agreement with previous TFM data on vascular SMCs [43,44], in the range of 1-10 μN, although previous data were not obtained on individual cells. We can also relate these traction force values to those from the study of Balaban et al. [51], which revealed force values of 10-30 nN for a single focal adhesion in human fibroblasts and 70 nN for cardiac myocyte when tested on 12 kPa substrates. They also mentioned that the orientation of the force was correlated with that of the focal adhesion and actin fibers. But the range of measured forces strongly varies with the experimental conditions and measurement method, as a 100-400 nN range was also reported for fibroblasts [69], and 10-800 nN for cardiomyocytes [70]. In the work of Tan et al. [45] on bovine airway SMCs, traction forces

were in a 10-60 nN range per adhesion site on a single fibronectin-coated post. But instead of removing the cells completely as we did in our study, they chose to disrupt components of the actin-myosin cytoskeleton or to stimulate its contraction by drug inducing.

As we measured traction forces on a relatively large number of cells, two major interesting observations could be drawn:

1. traction forces are variable and show an exponential distribution, with 40% to 80% of traction forces in the range 0-20 μN.

2. They depend on the substrate stiffness. The fraction of adhesion forces below 10 μN tend to decrease when the substrate stiffness increases, whereas the fraction of higher adhesion forces increases.

These two aspects (variability and stiffness dependent) an these distributions of cell adhesion are well predicted by the motor-clutch model of Chan & Odde [71]. Molecular clutches are the binding proteins constituting the focal adhesion. For every actin filament of the cytoskeleton, which is bound to the substrate, there is a traction force exerted through the myosin molecular motor onto the substrate via the associated clutch. In other words, molecular clutches link F-actin to the substrate and mechanically resist myosin-driven (motor) F-actin retrograde flow. When the binding fails, the traction force of the clutch comes to zero as shown in Fig. 7.

The variable behavior comes from the thermally activated kinetics of the clutches combined with the myosin-driven F-actin retrograde flow. We assume this flow is maintained at a constant speed v (Fig. 7). As explained by Chan et al. [71], the time it would take from clutch association until the adhesion force F is reached would write:

$$\Delta t = \frac{F}{k\, v} \tag{6}$$

where k is the stiffness of the substrate. As Δt is inversely proportional to k, the smaller the stiffness, the larger Δt. The probability of survival of a bond over a duration Δt would write:

$$P(\Delta t) = \frac{1}{T_{off}}\, exp\left(-\frac{\Delta t}{T_{off}}\right) \tag{7}$$

where T_{off} is the lifetime of the bond.

Then combining Eq. (7) and Eq. (8), the probability to be able to reach an adhesion force F is given by:

$$P(F) = \frac{1}{k\, v\, T_{off}}\, exp\left(-\frac{F}{k\, v\, T_{off}}\right) \tag{8}$$

This equation could be simplified and used as an exponential law as shown in Eq. (5), by taking:

$$\lambda = \frac{1}{k\, v\, T_{off}} \tag{9}$$

Eq. (8) shows that the probability of adhesion forces is going to satisfy an exponential distribution and that it depends on the stiffness of the substrate, exactly as observed in our experiments.

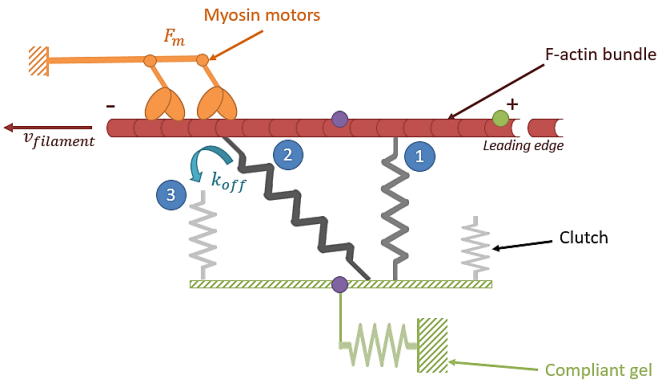

Figure 7: Schematic representation of the motor-clutch model. Once engaged (1), the clutch undergoes a load (2) and fail (3) cycle. The frequency of unbinding is named k_{off}

However, in the experiments, we observed that for stiffness increasing between 12 to 25 kPa, the change was not as significant as for stiffness increasing between 4 to 8 kPa for instance. This may be due to the fact that generally T_{off} is not a constant but it depends on the force. Indeed, according to Isabey et al. [72], the lifetime of a bond may be written such as:

$$T_{off} = T_0 \, exp\left(-\frac{F}{F_0}\right) \tag{10}$$

In other words, the rate of dissociation increases exponentially with the bonding force. Clutches with high forces have a very short lifetime. This effect may become significant for larger stiffness and should be investigated further.

4.3 Limitations

Cell traction force values have to be assessed carefully, because they strongly depend on the TFM process, namely the chosen scale and mechanical assumptions. The work of Zündel et al. [73] focused on the scale of the single focal adhesion and highlighted the results are misestimated when assuming a linear elastic substrate and neglecting the out-of-plane effects. They suggested to think about another way to characterize the mechanical behavior of the substrate, including the non-linearity, which seemed to improve the robustness of the reconstruction of the focal adhesion forces at this very high resolution. Our results may be immune to these artifacts as our study focuses on the cellular scale (i.e., several focal adhesions at the same measurement point), but in that case we have to keep in mind that we did not measure individual traction force values of each focal adhesion, but more the global SMC traction forces.

Moreover, for our current algorithm, we used the Boussinesq solution to model the theoretical displacement fields. Since the Boussinesq solution is valid for a half space, the study of Yang et al. showed it is less efficient for a thin plate [74]. In our case we proved with a 3D finite-element model that the Boussinesq solution was satisfactory, but the finite-element model considered the effect of a nodal force and not of a real SMC pulling on the gel. This could be refined in the future for a more thorough validation.

Another limitation is related to the analysis of single isolated cells. Cell to cell interactions may be important in arteries but they are not considered here. Moreover, extrapolation traction forces measured on 2D gels to 3D is very challenging and will require further work in order to represent the full 3D nature of cellular forces within the real ECM [75].

The type of coating could also have an influence on the phenotypic switching of the SMCs. In fact, the fibronectin tends to increase a change toward synthetic phenotype, but not the laminin [10,50]. But for collagen I, the density of the coating seems to influence the cellular area, which is reduced for high concentration of collagen I [50]. Consequently, the use of fully pre-coated gels with collagen I correlates

with the spindle shape we observed for our cells during TFM experiments. However, for our observation of the cellular architecture on fibronectin coating, we should compare our results on a laminin coating. Nevertheless, since the CYTOO^{TM} protocol requires few hours between seeding and fixation steps, the phenotypic change may have not the time to occur. We have to compare our results with unhealthy cells (that are suspected to be synthetic and so to involve a decreasing α-SMA expression). In this case, a change in α-SMA expression for the same fibronectin coating would be sufficient to show that the cells had not enough time to differentiate on a CYTOO^{TM} chip.

Finally, although we measured the traction forces for about 50 cells, the distribution of traction forces versus the gel stiffness would probably show significantly more consistent patterns if we had analyzed at least 500 cells, to increase the number of measures for each bar of the histogram. However, our experiments did not permit to achieve such sample size in a reasonable time and we believe that current results already show highly interesting trends despite the small sample size.

4 Conclusion

The contractile behavior of SMCs being an important determinant of growth, remodeling, and homeostasis in the aorta, we applied a TFM technique to measure traction forces of individual human aortic SMCs. The two major results were that: 1. SMC traction forces are variable and show an exponential distribution, with 40% to 80% of traction forces in the range 0-10 μN. 2. They depend on the substrate stiffness: the fraction of adhesion forces below 10 μN tend to decrease when the substrate stiffness increases, whereas the fraction of higher adhesion forces increases. As these two aspects (variability and stiffness dependence) and the distribution of traction forces can be predicted by the probabilistic motor-clutch model, we conclude that this model could be applied to predict the basal tone of SMCs. Further studies will consider stimulated contractility and primary culture of SMCs extracted from aneurysmal human aortic tissue in order to test the possible generalization of the motor clutch model to the diverse SMC states and to detect potential mechanobiological dysfunctions of aneurysmal SMCs.

Acknowledgements: This research was supported by the European Research Council (ERC grant Biolochanics, grant number 647067).

References

1. Cox TR, ErlerJT. Remodeling and homeostasis of the extracellular matrix: implications for fibrotic diseases and cancer. *Disease Models & Mechanisms* **2011**, 4(2): 165-178.
2. Humphrey JD. Cardiovascular Solid Mechanics. Springer New York, New York, NY. **2002.**
3. Humphrey JD, Schwartz MA, Tellides G, Milewicz, DM. Role of mechanotransduction in vascular biology: focus on thoracic aortic aneurysms and dissections. *Circulation Research* **2015**, 116(8): 1448-1461.
4. Hayashi K, Kamiya A, Ono K. Biomechanics: Functional Adaption and Remodeling. Springer Science & Business Media. **2012**.
5. Hong Z, Sun Z, Li M, Li Z, Bunyak F, Ersoy I et al. Vasoactive agonists exert dynamic and coordinated effects on vascular smooth muscle cell elasticity, cytoskeletal remodelling and adhesion. *Journal of Physiology* **2014**, 592(6): 1249-1266.
6. Mecham RP, Schwartz SM. Vascular Smooth Muscle Cell: Molecular and Biological Responses to the Extracellular Matrix (Biology of Extracellular Matrix Series). Academic Press. **1995**.
7. Lacolley P, Regnault V, Nicoletti A, Li Z, Michel JB. The vascular smooth muscle cell in arterial pathology: a cell that can take on multiple roles. *Cardiovascular Research* **2012**, 95(2): 194-204.
8. Reusch P, Wagdy H, Reusch R, Wilson E, Ives HE. Mechanical strain increases smooth muscle and decreases nonmuscle myosin expression in rat vascular smooth muscle cells. *Circulation Research* **1996**, 79(5): 1046-1053.
9. Thyberg J, Hedin U, Sjölund M, Palmberg L, Bottger BA. Regulation of differentiated properties and proliferation of arterial smooth muscle cells. *Arteriosclerosis (Dallas, Tex.)* **1990**, 10(6): 966-990.

10. Thyberg J, Blomgren K, Roy J, Tran PK, Hedin U. Phenotypic modulation of smooth muscle cells after arterial injury is associated with changes in the distribution of laminin and fibronectin. *Journal of Histochemistry and Cytochemistry: Official Journal of the Histochemistry Society* **1997**, 45(6): 837-846.
11. Wang JHC, Lin JS. Cell traction force and measurement methods. *Biomechanics and Modeling in Mechanobiology* **2007**, 6(6): 361-371.
12. Chen Z, Xu Y, Bujalowski P, Oberhauser AF, Boor PJ. *N*-(2-Aminoethyl) ethanolamine-induced morphological, biochemical, and biophysical alterations in vascular matrix associated with dissecting aortic aneurysm. *Toxicological Sciences* **2015**, 148(2): 421-432.
13. Tran T, McNeill KD, Gerthoffer WT, Unruh H, Halayko AJ. Endogenous laminin is required for human airway smooth muscle cell maturation. *Respiratory Research* **2006**, 7(1).
14. Arribas SM, Hinek A, González MC. Elastic fibres and vascular structure in hypertension. *Pharmacology & Therapeutics* **2006**, 111(3): 771-791.
15. Tsamis A, Krawiec JT, Vorp DA. Elastin and collagen fibre microstructure of the human aorta in ageing and disease: a review. *Journal of the Royal Society Interface* **2013**, 10(83).
16. Mao N, Gu T, Shi E, Zhang G, Yu L, Wang C. Phenotypic switching of vascular smooth muscle cells in animal model of rat thoracic aortic aneurysm. *Interactive CardioVascular and Thoracic Surgery* **2015**, 21(1): 62-70.
17. Rubbia L, Gabbiani G. Phénotype des cellules musculaires lisses artérielles et athérosclérose. *Médecine/Sciences* **1989**, 5(6): 389.
18. Owens GK, Rabinovitch PS, Schwartz SM. Smooth muscle cell hypertrophy versus hyperplasia in hypertension. *Proceedings of the National Academy of Sciences of the United States of America* **1981**, 78(12): 7759-7763.
19. Owens GK, Kumar MS, Wamhoff BR. Molecular regulation of vascular smooth muscle cell differentiation in development and disease. *Physiological Reviews* **2004**, 84(3): 767-801.
20. Chen J, Li H, SundarRaj N, Wang JHC. Alpha-smooth muscle actin expression enhances cell traction force. *Cell Motility and the Cytoskeleton* **2007**, 64(4): 248-257.
21. Brownstein AJ, Ziganshin BA, Kuivaniemi H, Body SC, Bale AE et al. Genes associated with thoracic aortic aneurysm and dissection: an update and clinical implications. *Aorta (Stamford)* **2017**, 5(1): 11-20.
22. Gillis E, Laer LV, Loeys BL. Genetics of thoracic aortic aneurysm: at the crossroad of transforming growth factor-β signaling and vascular smooth muscle cell contractility. *Circulation Research* **2013**, 113(3): 327-340.
23. Guo DC, Pannu H, Tran-Fadulu V, Papke CL, Yu RK et al. Mutations in smooth muscle alpha-actin (ACTA2) lead to thoracic aortic aneurysms and dissections. *Nature Genetics* **2007**, 39(12): 1488-1493.
24. Kuang SQ, Kwartler CS, Byanova KL, Pham J, Gong L et al. Rare, non-synonymous variant in the smooth muscle-specific isoform of myosin heavy chain, MYH11, R247C, alters force generation in the aorta and phenotype of smooth muscle cells. *Circulation Research* **2012**, 110(11): 1411-1422.
25. Regalado ES, Guo D, Prakash S, Bensend TA, Flynn K et al. Aortic disease presentation and outcome associated with ACTA2 mutations. *Circulation: Cardiovascular Genetics* **2015**, 8(3): 457-464.
26. Schildmeyer LA, Braun R, Taffet G, Debiasi M, Burns AE et al. Impaired vascular contractility and blood pressure homeostasis in the smooth muscle alpha-actin null mouse. *FASEB Journal: Official Publication of the Federation of American Societies for Experimental Biology* **2000**, 14(14): 2213-2220.
27. Milewicz DM, Trybus KM, Guo D, Sweeney HL, Regalado E et al. Altered smooth muscle cell force generation as a driver of thoracic aortic aneurysms and dissections. *Arteriosclerosis, Thrombosis, and Vascular Biology* **2016**.
28. Papke CL, Yamashiro Y, Yanagisawa H. MMP17/MT4-MMP and thoracic aortic aneurysms: OPNing new potential for effective treatment. *Circulation Research* **2015**, 117(2): 109-112.
29. Choudhury N, Bouchot O, Rouleau L, Tremblay D, Cartier R et al. Local mechanical and structural properties of healthy and diseased human ascending aorta tissue. *Cardiovascular Pathology* **2009**, 18(2): 83-91.
30. Pasta S, Rinaudo A, Luca A, Pilato M, Scardulla C et al. Difference in hemodynamic and wall stress of ascending thoracic aortic aneurysms with bicuspid and tricuspid aortic valve. *Journal of Biomechanics* **2013**, 46(10): 1729-1738.
31. Isselbacher EM. Thoracic and abdominal aortic aneurysms. *Circulation* **2005**, 111(6): 816-828.

32. Li C, Xu Q. Mechanical stress-initiated signal transduction in vascular smooth muscle cells *in vitro* and *in vivo*. *Cellular Signalling* **2007**, 19(5): 881-891.
33. Riches K, Angelini TG, Mudhar GS, Kaye J, Clark E et al. Exploring smooth muscle phenotype and function in a bioreactor model of abdominal aortic aneurysm. *Journal of Translational Medicine* **2013**, 11: 208.
34. Thyberg J, Blomgren K, Hedin U, Dryjski M. Phenotypic modulation of smooth muscle cells during the formation of neointimal thickenings in the rat carotid artery after balloon injury: an electron-microscopic and stereological study. *Cell and Tissue Research* **1995**, 281(3): 421-433.
35. Tremblay D, Cartier R, Mongrain R, Leask RL. Regional dependency of the vascular smooth muscle cell contribution to the mechanical properties of the pig ascending aortic tissue. *Journal of Biomechanics* **2010**, 43(12): 2448-2451.
36. Hayashi K, Naiki T. Adaptation and remodeling of vascular wall; biomechanical response to hypertension. *Journal of the Mechanical Behavior of Biomedical Materials* **2009**, 2(1): 3-19.
37. Hong Z, Reeves KJ, Sun Z, Li Z, Brown NJ, Meininger GA. Vascular smooth muscle cell stiffness and adhesion to collagen i modified by vasoactive agonists. *PLoS One* **2015**, 10(3): e0119533.
38. Stadler E, Campbell JH, Campbell GR. Do cultured vascular smooth muscle cells resemble those of the artery wall? If not, why not? *Journal of Cardiovascular Pharmacology* **1989**, 14(Suppl 6): 1-8.
39. Skalli O, Ropraz P, Trzeciak A, Benzonana G, Gillessen D et al. A monoclonal antibody against alpha-smooth muscle actin: a new probe for smooth muscle differentiation. *Journal of Cell Biology* **1986**, 103(6): 2787-2796.
40. Bellini C, Ferruzzi J, Roccabianca S, Di Martino ES, Humphrey JD. A microstructurally motivated model of arterial wall mechanics with mechanobiological implications. *Annals of Biomedical Engineering* **2014**, 42(3): 488-502.
41. Karnik SK. A critical role for elastin signaling in vascular morphogenesis and disease. *Development* **2003**, 130(2): 411-423.
42. Michel JB, Jondeau G, Milewicz DM. From genetics to response to injury: vascular smooth muscle cells in aneurysms and dissections of the ascending aorta. *Cardiovascular Research* **2018**, 114(4): 578-589.
43. Sazonova OV, Isenberg BC, Herrmann J, Lee KL, Purwada A et al. Extracellular matrix presentation modulates vascular smooth muscle cell mechanotransduction. *Matrix Biology* **2015**, 41: 36-43.
44. Balasubramanian L, Lo CM, Sham JSK, Yip KP. Remanent cell traction force in renal vascular smooth muscle cells induced by integrin-mediated mechanotransduction. *American Journal of Physiology-Cell Physiology* **2013**, 304(4): C382-C391.
45. Tan JL, Tien J, Pirone DM, Gray DS, Bhadriraju K et al. Cells lying on a bed of microneedles: an approach to isolate mechanical force. *Proceedings of the National Academy of Sciences* **2003**, 100(4): 1484-1489.
46. Goffin JM, Pittet P, Csucs G, Lussi JW, Meister JJ et al. Focal adhesion size controls tension-dependent recruitment of α-smooth muscle actin to stress fibers. *Journal of Cell Biology* **2006**, 172(2): 259-268.
47. Papke CL, Cao J, Kwartler CS, Villamizar C, Byanova KL et al. Smooth muscle hyperplasia due to loss of smooth muscle α-actin is driven by activation of focal adhesion kinase, altered p53 localization and increased levels of platelet-derived growth factor receptor-β. *Human Molecular Genetics* **2013**, 22(15): 3123-3137.
48. Hall A, Chan P, Sheets K, Apperson M, Delaughter C et al. Nanonet force microscopy for measuring forces in single smooth muscle cells of the human aorta. *Molecular Biology of the Cell* **2017**, 28(14): 1894-1900.
49. Landau LD, Lifshitz EM. Theory of Elasticity. Pergamon Press. **1989.**
50. Timraz SBH, Rezgui R, Boularaoui SM, Teo JCM. Stiffness of extracellular matrix components modulates the phenotype of human smooth muscle cells in vitro and allows for the control of properties of engineered tissues. *Procedia Engineering* **2015**, 110: 29-36.
51. Balaban NQ, Schwarz US, Riveline D, Goichberg P, Tzur G et al. Force and focal adhesion assembly: a close relationship studied using elastic micropatterned substrates. *Nature Cell Biology* **2001**, 3(5): 466-472.
52. Heo SJ, Szczesny SE, Kim DH, Saleh KS, Mauck RL. Expansion of mesenchymal stem cells on electrospun scaffolds maintains stemness, mechano-responsivity, and differentiation potential: mesenchymal stem cell isolation on nanofibrous scaffolds. *Journal of Orthopaedic Research* **2017**.

53. Athamneh AIM, Suter DM. Quantifying mechanical force in axonal growth and guidance. *Frontiers in Cellular Neuroscience* **2015**, 9.
54. Murray TR, Marshall BE, Macarak EJ. Contraction of vascular smooth muscle in cell culture. *Journal of Cellular Physiology* **1990**, 143(1): 26-38.
55. Raines EW, Ross R. Smooth muscle cells and the pathogenesis of the lesions of atherosclerosis. *British Heart Journal* **1993**, 69(1 Suppl): S30-S37.
56. Tran-Lundmark K, Tannenberg P, Rauch BH, Ekstrand J, Tran PK et al. Perlecan heparan sulfate is required for the inhibition of smooth muscle cell proliferation by all-*trans*-retinoic acid: AtRA inhibition of SMCS requires perlecan HS. *Journal of Cellular Physiology* **2015**, 230(2): 482-487.
57. Wanjare M, Kuo F, Gerecht S. Derivation and maturation of synthetic and contractile vascular smooth muscle cells from human pluripotent stem cells. *Cardiovascular Research* **2013**, 97(2): 321-330.
58. Ma X, Wang Y, Stephens NL. Serum deprivation induces a unique hypercontractile phenotype of cultured smooth muscle cells. *American Journal of Physiology* **1998**, 274 (5): C1206-C1214.
59. Anderson S, DiCesare L, Tan I, Leung T, SundarRaj N. Rho-mediated assembly of stress fibers is differentially regulated in corneal fibroblasts and myofibroblasts. *Experimental Cell Research* **2004**, 298 (2): 574-583.
60. Raines EW, Koyama H, Carragher NO. The extracellular matrix dynamically regulates smooth muscle cell responsiveness to PDGF. *Annals of the New York Academy of Sciences* **2000**, 902: 39-52.
61. Rzucidlo EM, Martin KA, Powell RJ. Regulation of vascular smooth muscle cell differentiation. *Journal of Vascular Surgery* **2007**, 45(6): A25-A32.
62. Hedin U, Bottger BA, Forsberg E, Johansson S, Thyberg J. Diverse effects of fibronectin and laminin on phenotypic properties of cultured arterial smooth muscle cells. *Journal of Cell Biology* **1988**, 107(1): 307-319.
63. Roy J, Tran PK, Religa P, Kazi M, Henderson B et al. Fibronectin promotes cell cycle entry in smooth muscle cells in primary culture. *Experimental Cell Research* **2002**, 273(2): 169-177.
64. Wagenseil JE, Mecham RP. Vascular extracellular matrix and arterial mechanics. *Physiological Reviews* **2009**, 89(3): 957-989.
65. Fujiwara T, Uehara Y. The cytoarchitecture of the medial layer in rat thoracic aorta: a scanning electron-microscopic study. *Cell and Tissue Research* **1992**, 270(1): 165-172.
66. Gomer CJ, Rucker N, Murphree AL. Differential cell photosensitivity following porphyrin photodynamic therapy. *Cancer Research* **1988**, 48(16): 4539-4542.
67. Megson IL, Flitney FW, Bates J, Webster R. Repriming of Vascular Smooth Muscle Photorelaxation is Dependent upon Endothelium-derived Nitric Oxide. *Endothelium* **1995**, 3(1): 39-46.
68. Andrews K., Mcguire J., Triggle C. A photosensitive vascular smooth muscle store of nitric oxide in mouse aorta: No dependence on expression of endothelial nitric oxide synthase. *British Journal of Pharmacology* **2003**, 138: 932-940.
69. Tong MH, Huang N, Zhang W, Zhou ZL, Ngan AHW et al. Multiphoton photochemical crosslinking-based fabrication of protein micropatterns with controllable mechanical properties for single cell traction force measurements. *Scientific Reports* **2016**, 6: 20063.
70. Hersch N, Wolters B, Dreissen G, Springer R, Kirchgeßner N et al. The constant beat: cardiomyocytes adapt their forces by equal contraction upon environmental stiffening. *Biology Open* **2013**, 2(3):351-361.
71. Chan CE, Odde DJ. Traction dynamics of filopodia on compliant substrates. *Science (New York, N.Y.)* **2008**, 322(5908): 1687-1691.
72. Isabey D, Pelle G, André Dias S, Bottier M, Nguyen NM et al. Multiscale evaluation of cellular adhesion alteration and cytoskeleton remodeling by magnetic bead twisting. *Biomechanics and Modeling in Mechanobiology* **2016**, 15(4): 947-963.
73. Zündel M, Ehret AE, Mazza E. Factors influencing the determination of cell traction forces. *PLoS One* **2017**, 12(2): e0172927.
74. Yang Z. Validation of the Boussinesq equation for use in traction field determination. *Computer Methods in Biomechanics and Biomedical Engineering* **2011**, 14(12): 1065-1070.

75. Legant WR, Choi CK, Miller JS, Shao L, Gao L et al. Multidimensional traction force microscopy reveals out-of-plane rotational moments about focal adhesions. *Proceedings of the National Academy of Sciences* **2013**, 110(3): 881-886.

76. Blaber J, Adair B, Antoniou A. Ncorr: open-source 2D digital image correlation matlab software. *Experimental Mechanics* **2015**, 55(6): 1105-1122.

77. Pan B, Xie H, Wang Z. Equivalence of digital image correlation criteria for pattern matching. *Applied Optics* **2010**, 49(28): 5501-5509.

78. Croeze A., Pittman L., Reynolds W. Nonlinear Least-Squares Problems with the Gauss-Newton and Levenberg-Marquardt Methods. **2012**.

Appendix A. Fluorescent staining Protocol and Dyes

In order to observe the cell structure, we used CYTOO^{TM} Starter chips that consist in micro-patterned coverslides having four different shapes and three different sizes. Since the patterns are coated with fibronectin, cells adhere and adapt their shape to them. The CYTOO^{TM} chips also contain a thick fibronectin line where the cells adhere randomly.

The Fluorescent Microscopy (FM) technique constitutes a powerful technique to enable observations at the cellular (between 10-100 µm) and subcellular (1-10 µm) scales with a precise localization of the different cellular components under the membrane. However, elements are observable only if previously stained with fluorophores. Each fluorophore activated at its excitation wavelength emits in return a fluorescent light at the emission wavelength (respectively λ_{Ex} and λ_{Em} in Tab. A1 below).

Table A1: Characteristics of the different fluorescent dyes used for the study

Actin (Cytoskeleton)	Direct (phalloidine)	Rhodamine (red)	554	579
α-SMA	Indirect (ACI mouse + ACII anti-mouse conjugué)	AlexaFluor 488 (green)	554 490	568 525
DNA (nucleus)	Direct (Hoescht)	Hoescht (blue)	350	470
Fibronectin (CYTOO^{TM})	Already stained	Far red 650	640	658
Microbeads (Matrigen^{TM})	Already stained	Yellow-Green (Life Technologies)	505	515

Some fluorophores can link directly onto their receptor like Phalloidin onto filamentous actin (F-actin) in the cytoskeleton and Hoescht on DNA in the nucleus. If Hoescht naturally emits a blue fluorescent light, Phalloidin has to be combined with a fluorescent tag (Rhodamin in our case). Other fluorophores need to be combined to antibodies notably for α-SMA staining in order to characterize SMC contractility. When antibodies are used for fluorescent staining (immunofluorescence), the fluorescence can be direct (with only one conjugated antibody against the cellular component to stain) or indirect (involving a non-conjugated primary antibody against the component to stain and a conjugated secondary antibody against the primary one). The list of all the fluorescent dyes used in this study with their characteristics is reported in Tab. A1.

For the initial observation of their morphology, cells were previously fixed with 4% Paraformaldehyde (PFA) in PBS once they had adhered and spread across the CYTOO^{TM} fibronectin coating which were placed in a 35mm Petri dish. Since antibodies could not penetrate the porous membrane, it was necessary to render it permeable with a 0.1% TritonX100 in PBS solution. Then, PBS with 1% Bovine Serum Albumine (BSA) was used as a blocking reagent in order to avoid unspecific bindings. Both the Hoescht and the Phalloidin fluorophores were diluted at 1/1000 in PBS for respectively 10 min and 1 hour. For α-SMA staining, we let the primary antibody at 1/200 and then the secondary at 1/500 for 1 hour each. The stained sample was kept away from light in PBS until achieving the TFM experiments which took place 1 day after (fluorophores tend to fade away in PBS after some days).

Only the Hoescht fluorophore can be used on living cells as it can penetrate into the cell membrane and it is much less toxic than phalloidin. Accordingly, we used it for our TFM experiments in order to localize the living cells on the hydrogels (which was difficult otherwise). Generally, we had not to stain the nucleus to see the cells, because they were visible in bright light. And even if Hoescht may be cytotoxic in the long term, our experiments lasting less than 4 hours, it was better than frequent light exposure as SMCs showed a significant photosensitivity.

Appendix B. DIC Algorithm

In a first step, the ROI was divided into NxM square subsets. Each subset, denoted Ω_{ij}, was labelled by the coordinates of its center in the reference configuration, denoted (x_i, y_j), with $1 \leq i \leq N$ and $1 \leq j \leq M$. The 2D deformation field across a given subset, from the reference to a deformed configuration was written such as:

$$\begin{aligned} u(x,y) &= u_{ij} + (x - x_i)u_{ij,x} + (y - y_j)u_{ij,y} \\ v(x,y) &= v_{ij} + (x - x_i)v_{ij,x} + (y - y_j)v_{ij,y} \end{aligned} \tag{10}$$

where $u_{ij} = u(x_i, y_j)$ and $v_{ij} = v(x_i, y_j)$ are the displacement components at (x_i, y_j) and $u_{ij,x}$, $u_{ij,y}$, $v_{ij,x}$ and $v_{ij,y}$ are four regularization parameters to be determined, permitting a more precise description of the subset deformation.

The basic principle of DIC is the following. In the reference configuration the image can be represented by the intensity level function $f(x,y)$, and in the deformed state by the intensity level function $g(x,y)$. Functions f and g were reconstructed continuously for any (x,y) position from the intensity level of each pixel using interpolation with biquintic B-splines. The conservation of intensity was assumed, yielding: $f(x,y) = g(x+u, y+v)$. The objective was to find unknowns u_{ij}, v_{ij}, $u_{ij,x}$, $u_{ij,y}$, $v_{ij,x}$ and $v_{ij,y}$ for each subset maximizing the cross-correlation between $f(x,y)$ and $g(x+u, y+v)$. We represented the set of unknowns for a given subset Ω_{ij} with a vector denoted $\boldsymbol{p}_{ij}$.

We used the NCorr open source 2D Digital Image Correlation (DIC) Matlab® toolbox [76]. The *NCorr* algorithm is an iterative algorithm seeking at each iteration for $\boldsymbol{p}_{ij}^{(n+1)} = \boldsymbol{p}_{ij}^{(n)} + \Delta\boldsymbol{p}_{ij}^{(n)}$ where $\Delta\boldsymbol{p}_{ij}^{(n)}$ maximizes the normalized cross-correlation coefficient:

$$\mathcal{C}^{(n)}(\Delta\boldsymbol{p}_{ij}) = \frac{\iint_{\Omega_{ij}} \left(f\left(x-u\left(\Delta\boldsymbol{p}_{ij}^{(n)}\right), y-v\left(\Delta\boldsymbol{p}_{ij}^{(n)}\right)\right) - \bar{f}_{ij}\right)\left(g\left(x+u\left(\boldsymbol{p}_{ij}^{(n)}\right), y+v\left(\boldsymbol{p}_{ij}^{(n)}\right)\right) - \bar{g}_{ij}\right) \mathrm{d}x\mathrm{d}y}{\sqrt{\iint_{\Omega_{ij}} \left(f\left(x-u\left(\Delta\boldsymbol{p}_{ij}^{(n)}\right), y-v\left(\Delta\boldsymbol{p}_{ij}^{(n)}\right)\right) - \bar{f}_{ij}\right)^2 \mathrm{d}x\mathrm{d}y \iint_{\Omega_{ij}} \left(g\left(x+u\left(\boldsymbol{p}_{ij}^{(n)}\right), y+v\left(\boldsymbol{p}_{ij}^{(n)}\right)\right) - \bar{g}_{ij}\right)^2 \mathrm{d}x\mathrm{d}y}} \tag{11}$$

where $\bar{f}_{ij}$ and $\bar{g}_{ij}$ were the mean grayscale values for the Ω_{ij} subset [77]. The non-linear optimization was achieved with the Gauss-Newton method, consisting in solving the following linear equation:

$$\nabla\nabla\mathcal{C}^{(n)}(0)\Delta\boldsymbol{p}_{ij}^{(n)} = -\nabla\mathcal{C}^{(n)}(0) \tag{12}$$

where the derivation of the Hessian $\nabla\nabla\mathcal{C}^{(n)}(0)$ and the gradient $\nabla\mathcal{C}^{(n)}(0)$ are documented in [78] The process was initialized with $\boldsymbol{p}_{ij}^{(0)} = \left\{u_{ij}^{(0)}, v_{ij}^{(0)}, 0, 0, 0, 0\right\}$ where $u_{ij}^{(0)}$ and $v_{ij}^{(0)}$ are integer numbers of pixels maximizing the cross correlation between reference and deformed images.

We defined a ROI surrounding each SMC focal adhesion where the gel showed deformations during the recorded experiments (Fig. 1(B)). This means that we had a ROI surrounding each location where we had a traction force to be estimated. We used a subset size of 25 pixels to assess the displacement fields in each ROI. The strain fields were derived from the displacement fields using a finite-difference scheme (Fig. 1(B)).

Appendix C. Full TFM Data on 24-Well Plates

Table C1: Mean traction force values measured on the 24-well plates, number of measurements (NB), mean value and standard deviation σ according to the different gels stiffness

E(kPa)	4	8	12	25
F(N)	4.94E-06	3.86E-04	7.58E-05	3.31E-04
	4.58E-06	7.32E-06	5.15E-06	4.60E-05
	2.53E-06	8.36E-06	5.48E-05	6.40E-05
	2.53E-06	1.68E-05	6.37E-06	1.98E-05
	8.29E-06	7.86E-06	7.80E-06	1.59E-05
	1.00E-06	8.38E-06	1.86E-05	1.56E-05
	5.13E-06	9.79E-06	1.47E-04	8.24E-06
	1.16E-05	1.48E-05	3.09E-06	7.57E-06
	9.86E-07	9.64E-06	4.63E-05	2.95E-06
	2.61E-06	3.31E-06	9.32E-06	3.49E-05
	1.22E-06	1.73E-06	4.89E-06	2.97E-06
	6.96E-06	2.34E-06	1.15E-05	2.13E-05
	6.28E-06	6.62E-05	5.31E-06	2.28E-05
	1.40E-06	1.19E-05	2.66E-04	8.25E-06
	9.66E-07	6.94E-06	3.37E-05	8.31E-06
	7.43E-06	3.08E-05	2.61E-05	4.37E-06
	8.89E-06	1.73E-05	7.72E-05	1.62E-06
	7.95E-06	1.66E-05	1.44E-05	2.08E-05
	2.64E-06	2.99E-04	6.87E-06	2.68E-05
	9.88E-07	5.09E-06	2.20E-05	2.08E-04
	3.76E-07	5.35E-06	1.58E-05	1.51E-05
	8.93E-06	1.13E-05	1.42E-05	2.02E-04
	8.19E-06	2.51E-05	1.51E-05	6.38E-06
	6.20E-06	1.07E-04	2.80E-05	1.47E-05
	7.90E-06	1.80E-04	3.57E-06	3.72E-06
	2.36E-06	6.55E-06	4.91E-05	8.73E-06
	8.25E-06	1.09E-05	7.77E-06	2.73E-06
	3.06E-06	6.41E-07	1.56E-05	2.60E-05
	6.80E-06	2.02E-05	1.15E-05	2.21E-06
	1.65E-05	5.30E-05	3.31E-05	1.45E-06
	7.76E-05	3.62E-06	3.07E-06	2.63E-06
	8.32E-06	7.65E-05	1.48E-05	3.89E-06
	8.16E-06	2.41E-04	3.83E-06	
	4.77E-06	1.26E-05	1.61E-05	
	4.13E-06	3.13E-06	2.36E-05	
	3.58E-06	1.02E-05	2.70E-06	
	1.66E-05	1.86E-05	7.68E-06	
	7.94E-06	2.14E-06	4.38E-06	
	4.68E-05	1.10E-06	1.04E-05	
	5.18E-06	7.61E-06	5.27E-06	
	3.19E-06	7.36E-06	1.38E-05	
	1.24E-05	6.09E-06	3.20E-06	
	5.30E-05	5.71E-06	8.52E-06	

	8.64E-05	1.82E-06	4.76E-06	
	1.79E-06	3.17E-06		
	6.70E-07	3.39E-06		
		2.42E-06		
		4.94E-06		
		1.24E-05		
NB	46	49	44	32
Mean F (µN)	10.83	36.21	26.30	36.27
σ (µN)	18.29	78.31	45.44	72.63